

GT2022-82298

HEAT TRANSFER AND PRESSURE LOSS OF ADDITIVELY MANUFACTURED INTERNAL COOLING CHANNELS WITH VARIOUS SHAPES

Alexander J. Wildgoose and Karen A. Thole

Department of Mechanical Engineering
Pennsylvania State University
University Park, PA, USA

ABSTRACT

Additive manufacturing (AM) provides the ability to fabricate highly customized internal cooling passages that are relevant to gas turbine components. This experimental study examines the pressure loss and heat transfer performance of a range of fundamental channel shapes that were produced using direct metal laser sintering. Circular, hexagonal, pentagonal, elliptical, diamond, square, rectangular, trapezoidal, and triangular channel cross-sections were investigated. To maintain the same convective surface area between shapes, the wetted perimeters of the channel cross-sections were kept constant. Parallel computational fluid dynamic simulations were performed to understand the relationships in cooling performance between several channel shapes. Several characteristic length scales were evaluated to scale the pressure loss and heat transfer measurements. Among the channel shapes investigated, the diamond channel showed the lowest Nusselt number and friction factor. The pentagon exhibited a similar Nusselt number as the circular channel despite having a lower friction factor. There was no difference in scaling the friction factor or Nusselt number results of the different channels shapes between using the square root of cross-sectional area compared to hydraulic diameter as the characteristic length scale.

NOMENCLATURE

A_c	cross-sectional flow area
A_s	surface area
D_h	hydraulic diameter, $4A_c/p$
f	Darcy friction factor, $f = \Delta P \frac{D_h}{L} \frac{2}{\rho u_{mean}^2}$
h	convective heat transfer coefficient, $h = \frac{Q_{in,heater} - \sum Q_{loss}}{A_s \Delta T_{lm}}$
K_s	sandgrain roughness
k	thermal conductivity
L	channel length
\dot{m}	mass flowrate
Nu_{D_h}	Nusselt number, hD_h/k_{air}
$Nu_{\sqrt{A_c}}$	Nusselt number, $h\sqrt{A_c}/k_{air}$
p	channel perimeter
P	static pressure
Pr	Prandtl number
Q_{air}	$Q_{air} = \dot{m} C_p (T_{out} - T_{in})$

Q_{heat}	energy from heaters
R_a	arithmetic mean roughness
Re_{D_h}	Reynolds number, $u_{mean} D_h/\nu$
$Re_{\sqrt{A_c}}$	Reynolds number, $u_{mean}\sqrt{A_c}/\nu$
S	channel pitch distance
T	temperature
T_{LM}	log-mean temperature, $\Delta T_{LM} = \frac{(\Delta T_{in} - \Delta T_{out})}{\ln\left(\frac{T_s - T_{in}}{T_s - T_{out}}\right)}$
T_{mean}	mass average temperature
U_{mean}	mass average velocity
Z_{ref}	reference surface plane
Z_{surf}	roughness height

Greek

ρ	fluid density
ν	kinematic viscosity
Θ	nondimensional temperature
σ	standard deviation

Subscripts

act	actual dimension calculated from CT Scan
des	design intent dimension
in	inlet condition
out	exit condition
s	surface condition
w	wall condition

INTRODUCTION

As additive manufacturing (AM) becomes more common in the fabrication of gas turbine components, engineers will begin to better use the added design freedom to construct more complex and higher performing cooling schemes as compared to those that are traditionally investment casted. Prior internal cooling research has looked into the cooling performance of additively made lattice structures [1,2], wavy channels [3], and rectangular/circular [4–6] cross-sectional channels. A broader focus on the impact of simplistic polygonal-shaped channels on heat transfer and pressure losses has not been thoroughly investigated. The ability to predict the pressure loss and heat transfer of different channel shapes accurately is important for a range of applications. The channel shape can impact the

secondary flows resulting in differences to pressure loss and heat transfer. Several researchers [7–10] have investigated a variety of channels with different cross-sections and saw that using length scales other than hydraulic diameter better scaled cooling performance. The objective of this study is to make use of the additive process to manufacture various channel shapes to determine how the resulting heat transfer and pressure losses are impacted as well as how to best scale the results.

LITERATURE REVIEW

Multiple studies have evaluated the pressure loss and heat transfer of various internal channel shapes [7–9,11–13]. As reported by Kays and Crawford [14], hydraulic diameter is predominantly used as a characteristic length to scale the pressure loss and heat transfer of different cross-sectional channel shapes. However, several studies [7,13,15] have found discrepancies when using hydraulic diameter to scale pressure loss for hydraulically smooth cross-sectional shapes. Most notably, Duan et al. [7] showed that when using hydraulic diameter as the length scale for friction factor and Reynolds number, a triangular cross-section can have up to a 30% lower friction factor compared to a circular cross-section thereby indicating that the hydraulic diameter may not be accurately scaling the data. In addition, Jones [15] found that for different aspect ratio rectangular channels the friction factor can be up to 37% higher or 23% lower than a circular channel. These studies emphasize the struggle that hydraulic diameter has as a characteristic length to adequately scale the pressure loss of different channel cross-sections. Consequently, Duan et al. [7] showed that using other length scales, such as the square root of cross-sectional area reduces the scatter in friction factor for various channel shapes compared to hydraulic diameter.

Despite the fewer number of experimental heat transfer measurements relative to pressure loss, studies such as Duan [16] and Leung et al. [13] showed that there can be a range of Nusselt numbers between different channel shapes when using hydraulic diameter as the characteristic length scale. In particular, Leung et al. [17] found that Nusselt number for range of apex angles of triangular ducts can be as much as 29% lower than the Dittus-Boelter Nusselt number correlation. The numerical results from Wang et al. [10] show that the Nusselt number calculated using hydraulic diameter of an equilateral triangle can be 28% different from predictions using traditional Nusselt number correlations developed for circular channels. Similar to the scaling of friction factor, Duan [16] found that using the square root of cross-sectional area scaled Nusselt number for a range of channel shapes better than that of hydraulic diameter. However, due to the lack of available noncircular turbulent heat transfer data the heat transfer results from Duan [16] was generated using the Colburn analogy and not experimental data.

The previous studies mentioned for both pressure loss and heat transfer mainly evaluated a select few of channel shapes such as trapezoidal, rectangular, and triangular cross-sections. The limited amount of noncircular channel shape measurements of pressure loss and heat transfer are possibly a result limited manufacturability. In contrast, AM provides for the fabrication of channel shapes that were not available for the previous studies. A significant portion of AM channel literature that have fabricated different channel shapes focus more on channel deformation [18–21] rather than pressure losses or convective heat transfer. A comprehensive review from Thole et al. [22] provides an overview of cooling performance of additively made channels.

The portion of available AM cooling performance datasets includes a small range of channel shapes such square, rectangular, and circular cross-sections compared to the shapes that have been evaluated in non-AM studies. Subsequently, there is limited knowledge about the scalability of pressure loss or heat transfer using characteristic length scales other than hydraulic diameter.

This study aims to provide additional experimental pressure loss and heat transfer measurements for a range of different channel shapes that have not been evaluated in the literature. Additionally, this paper addresses the scaling of friction factor and Nusselt number results with a characteristic length scale other than hydraulic diameter for polygonal shaped channels. Numerical simulations were performed on select channel shapes to provide a further understanding of the heat transfer performance between channel cross-sections.

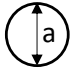
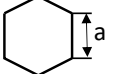
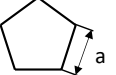
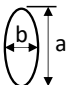
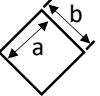
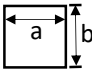
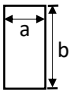
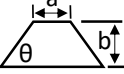

DESCRIPTION OF TEST COUPONS

To assess the impact channel shape has on the pressure loss and convective heat transfer, a variety of straight channel shapes were fabricated using direct metal laser sintering (DMLS). Nine channel shapes were selected for evaluation and are specified in Table 1. The nine channel shapes were designed to maintain the same cross-sectional perimeter and coupon length to guarantee the same convective heat transfer surface area. The design perimeter for each channel was chosen to match a circular diameter of 1.5 mm giving a perimeter of 4.8 mm.

As seen in Figure 1, each test coupon was designed to have nine channels. The channel pitch spacing (S), as seen in Figure 1, was controlled such that the fin efficiency between channels was greater than 95% to fulfill the constant surface temperature boundary condition during heat transfer measurements. The length-to-hydraulic diameter ratios of the channels were between $33 < L/D_h < 54$, which meets fully developed conditions.

The channels were fabricated using a 90° build direction where the streamwise axis of the channel is perpendicular to the surface of the build plate to give the least amount of deformation from their design intent. There were no supports placed inside the channels. Additionally, the channel pitch was designed to limit channel deformation attributed to the proximity of nearby channels. The coupons were fabricated using an EOS-M280 powder bed fusion machine in Inconel 718 (IN718) with a 40-micron layer size. The recycled powder, supplied by EOS, was sieved through a filter to a nominal 40-micron powder size before use. To lower the chance of particle drag caused by a damaged re-coater blade impacting the coupons, the coupons were angled 3° between their streamwise channel axis and the recoater blade direction as recommended by EOS [23]. Coupons were grouped to limit differences in surface roughness caused by the build location on a substrate as seen in literature [4,24]. To maintain consistency with past literature [4–6], all coupons used the recommended EOS processing parameters, outlined in Table 2, for a 40-micron layer size in IN718 with wall contouring. The calibration parameters in Table 2 were carried out using the manufactures procedures [23]. Loose powder was removed from the internal channels and supports prior to heat treatment. The coupons were solution annealed while attached to the substrate to remove residual stress as recommended by standard EOS heat treatment procedures for Inconel 718 [23]. After heat treatment, a wire electrical discharge machine removed the coupons off the substrate and remove supports.

Table 1. Geometric Specifications for Coupons Sharing a Constant Perimeter ($P_{des} = 4.79 \text{ mm}$)

Coupon Name	$D_{h, act}$ [μm]	$A_{c, act}$ [μm^2] $\cdot 10^7$	$\frac{D_{h, act}}{D_{h, des}}$	$\frac{p_{act}}{p_{des}}$	$\frac{A_{c, act}}{A_{c, des}}$	$\frac{S_{des}}{D_{h, des}}$	$\frac{R_a}{D_{h, act}}$	Geometry Aspect Ratios [μm]
Circle	1590	1.81	1.04	1.06	1.10	1.43	0.0074	$a = D_h$ 
Hexagon	1497	1.68	1.08	1.04	1.13	1.57	0.0037	$a = 797.96$ 
Pentagon	1428	1.60	1.08	1.04	1.13	1.66	0.0048	$a = 957.56$ 
Ellipse	1340	1.51	1.05	1.05	1.09	1.66	0.0049	$a/b = 2$ 
Diamond	1314	1.46	1.10	1.03	1.13	1.84	0.0037	$a/b = 1$ 
Square	1283	1.50	1.07	1.09	1.17	1.80	0.0133	$a/b = 1$ 
Rectangle	1200	1.34	1.13	1.04	1.17	1.99	0.0060	$a/b = 2$ 
Trapezoid	1145	1.32	1.11	1.07	1.19	2.16	0.0148	$a/b = 0.8$ $\Theta = 60^\circ$ 
Triangle	1047	1.19	1.14	1.05	1.20	2.38	0.0114	$\Theta = 60^\circ$ 

CHARACTERIZATION OF CHANNEL SHAPES

Characterizing the as-built quality and resolving the internal surface morphology are important in evaluating impacts on pressure loss and heat transfer. The coupons were nondestructively evaluated using a computed x-ray tomography (CT scan) method to measure as-built geometries and surface roughness of the channels. To resolve the entire internal surface of all the channels, all coupons were CT scanned at a 35 micron spatial resolution (voxel size). A commercial software [25] was used to capture the internal surface through selectively filtering gray scale values obtained from the volumetric CT scan measurements. Through interpolation the same software is able to resolve $1/10^{\text{th}}$ of the original voxel size [26].

Channel cross-sectional areas, perimeters, and hydraulic diameters were calculated using an in-house code to analyze 1,200 cross-sectional CT image slices taken along the streamwise axis of the coupon. Pixels in each free space were summed to calculate cross-sectional area while the number of pixels along the border of a channel slice was recorded as the perimeter. Each perimeter and cross-sectional area were averaged to determine a mean hydraulic diameter. Regardless of channel shape, the channel cross-sectional area deviated more from the design intent compared to perimeter as seen in Table 1. The cross-sectional area, perimeter, and hydraulic diameter are larger than the design intent for all the channel shapes. This result is similar to previous circular channel literature at the same build direction [4,6].

Even though each channel shape has larger dimensions for the as-built geometry than the design intent, the variation in geometric parameters are different between the channel shapes as seen in Figure 2. A histogram for each of the CT slices showing

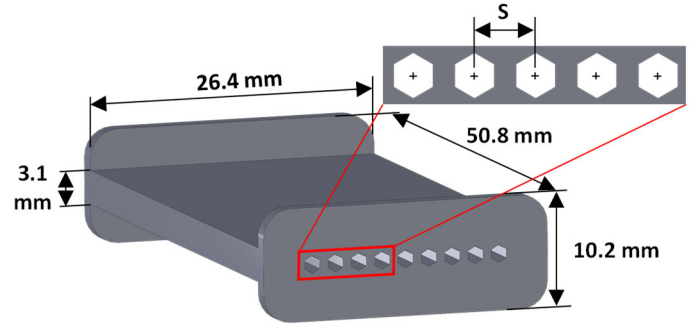


Figure 1. Schematic of coupon dimensions used for experimental testing.

Table 2. Processing Parameters for AM Coupons

Parameter	Value
Material	Inconel 718
Layer thickness	0.04 mm
Material setting	IN718 040 211 Performance
Material scaling X	0.12%
Material scaling Y	0.12%
Beam offset	0.12 mm

the distribution of hydraulic diameter is shown in Figure 2 as compared with the design intent (vertical lines). Clearly seen in Figure 2, the as-built diameter is larger than the design intent for all channel shapes. The square, trapezoid, and triangle contain a wider distribution of hydraulic diameter compared to the ellipse, circle and diamond indicating different channel shapes not only deviate from design intent but also contain variations in their geometric dimensions.

The standard deviations of each channel geometry are shown in Figure 3(a-c). Distinct channel shapes exhibit wider distributions in geometric dimensions as seen in the 3σ deviations of perimeter, cross-sectional area, and hydraulic diameter. As seen in Figure 3(a), the square and trapezoid have the largest variation in hydraulic diameter while the ellipse, diamond, and hexagon contain the smallest variation. There is more variation in perimeter between the different channel shapes as compared to cross-sectional area. As observed in Figure 3(b,c), there is a 140% difference between the highest and lowest 3σ deviation of perimeter while there is a 53% difference between the highest and lowest 3σ deviation of cross-sectional area. The trapezoid, square, and triangle exhibit the largest variation while the ellipse, diamond, hexagon, and circle show the least amount of variation across all geometric dimensions as seen in Figure 3(a-c).

The square and diamond channels share the same design intent geometric dimensions with the only difference being the streamwise rotation of the channel. The range of hydraulic diameters is wider for the square as compared to the diamond seen in Figure 3(a). Channel cross-sectional slices in Figure 4(e,f) show that the square contains more surface deformations relative to the diamond which confirms the variations in hydraulic diameter exhibited in Figure 3(a).

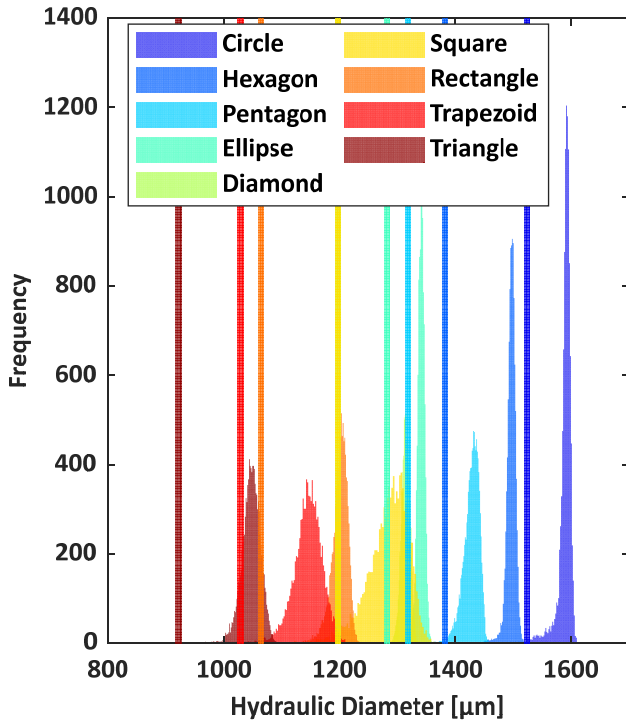


Figure 2. Distribution of hydraulic diameter along with design intent calculated from CT scans of the different channel shapes.

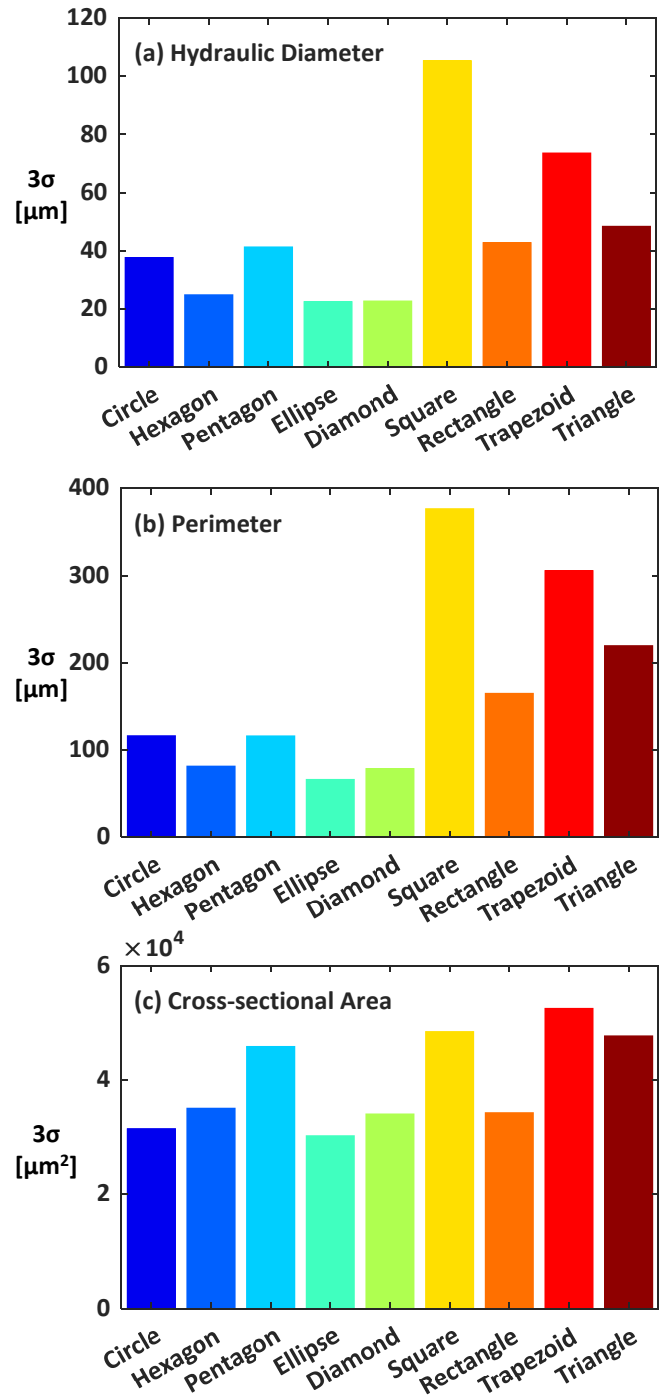


Figure 3. 3σ deviations of hydraulic diameter (a), perimeter (b), and cross-sectional area (c) of the different channel shapes.

Also shown in Figure 4(a-i) are channel cross-sections at different axial distances along the streamwise length of the coupon. Centroids at each axial slice, Figure 4(a-i), indicate the circle, ellipse, and diamond display the least amount of difference between centroids compared to the square, rectangle, trapezoid, and triangle. The wider spread of centroids of the square, trapezoid, and triangle shapes, seen in Figure 4(f,h,i), are consistent with those same shapes exhibiting larger variations in hydraulic diameter compared to the ellipse, diamond, and circle as shown in Figure 3(a).

Accompanied in Figure 4(a-i) is a 12, 3, 6, and 9 o'clock compass which is used to indicate the specific surface orientation

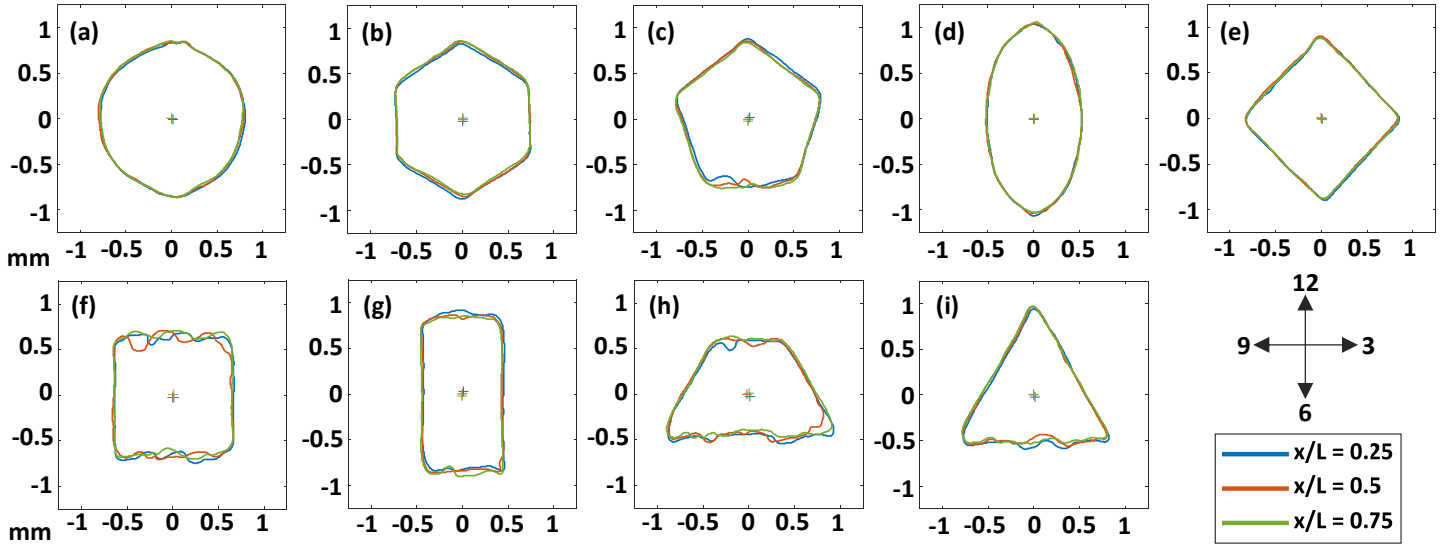


Figure 4. Axial slices of channel shapes (circle (a), hexagon (b), pentagon (c), ellipse (d), diamond (e), square (f), rectangle (g), trapezoid (h), and triangle (i) sharing a constant design intent perimeter of 4.79 mm fabricated at the 90° build direction.

within a channel cross-section. As seen in the Figure 4(a-i) slices, surfaces that are at the 12 o'clock and 6 o'clock (horizontal) orientation exhibit sizable surface deformations compared to any other surface orientations. This effect is visibly seen in the slices of the square and diamond, where the square's 12 and 6 o'clock surfaces contain more noticeable surface deformations compared to the diamond surfaces even though both shapes share the same design intent geometry.

Quantitatively when examining the square shape, minimal surface deformations occur at the 3 and 9 o'clock orientation relative to the larger surface deformations seen at the 12 and 6 o'clock surfaces. The reason for these differences in surface roughness has been found by Wildgoose et al. [27] to be a factor of wall thickness and build location.

ROUGHNESS QUANTITIES

Surface roughness, specifically the arithmetic mean roughness (R_a), further characterizes the channel surface. The arithmetic mean roughness provides the average surface deviation from a reference as described in equation (1).

$$R_a = \frac{1}{n} \sum_{i=1}^n |z_{surf} - z_{ref}| \quad (1)$$

All channel shapes, except for the circle and ellipse due to their inherent surface curvature, used a plane that was fitted to

each surface using a Gaussian distribution in order to serve as the reference value, z_{ref} , when calculating the arithmetic mean roughness measurements. The average difference between the plane and the channel surface was recorded as the arithmetic mean roughness. An ellipsoid was fitted using a linear least square regression method to each axial slice to serve as a reference line for the circle and ellipse. This follows a similar procedure outlined in Wildgoose et al. [6] and Klingaa et al. [28].

Shown in Figure 5, the arithmetic mean roughness value for the circular channel is consistent with size and magnitude of previous AM circular channel literature [6,28–30] despite being larger in hydraulic diameter. In Figure 5 channel surfaces are color coded to the individual bars. The arithmetic mean roughness is higher on the 12 and 6 o'clock surfaces compared to all other surface orientations. Nearly all surfaces that are not at the 6 or 12 o'clock orientation contains the same arithmetic mean roughness value.

The 3 and 9 o'clock channel surfaces of the hexagon, square, and rectangular shapes share a similar arithmetic mean roughness. When comparing the rounded channels, both the circle and ellipse contain protrusions at the 6 and 12 o'clock locations seen in Figure 4(a,d), with the circle containing the larger deviations.

The arithmetic mean roughness for the surfaces of each channel shape in Figure 5 is averaged and displayed in Figure 6. The averaged arithmetic mean roughnesses in Figure 6 are

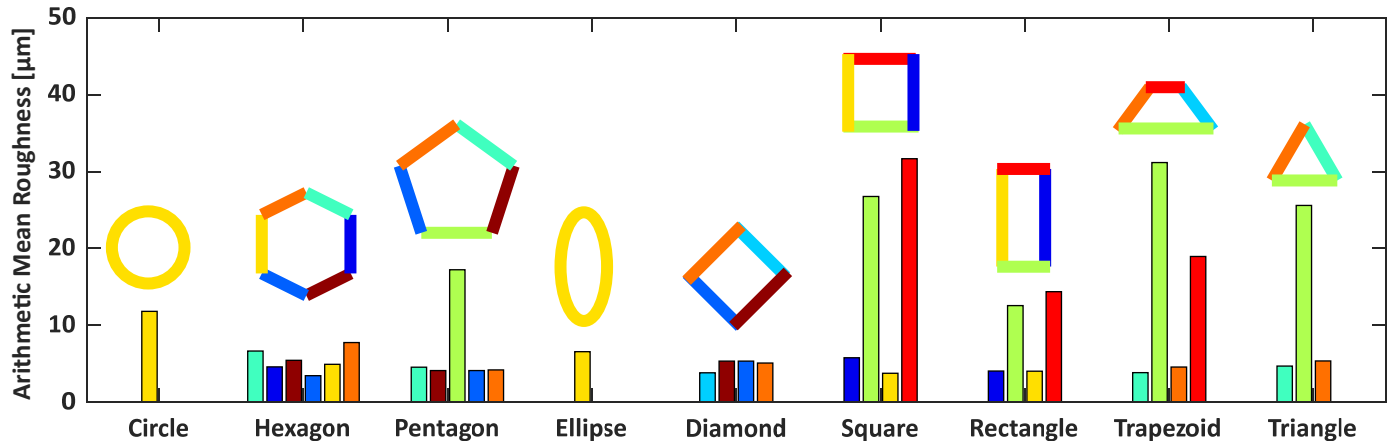


Figure 5. Arithmetic mean roughness, R_a , from CT scan data of multiple surfaces among the different channel shapes which are at the same surface orientation as Figure 4(a-i).

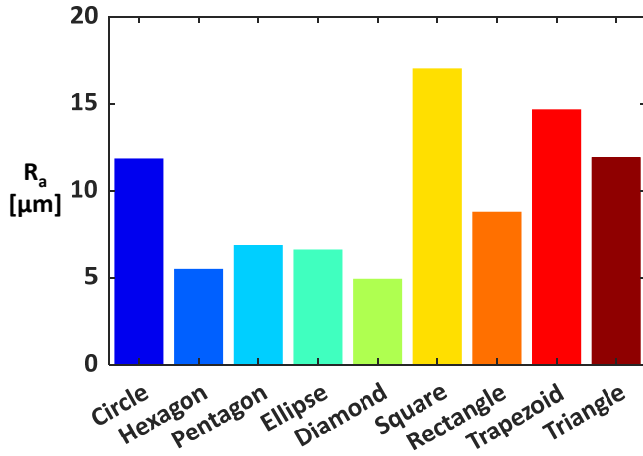


Figure 6. Area average arithmetic mean roughness of the different channel shape surfaces weighted by the design intent surface area.

weighted by the surface area of the channel shapes. Channel shapes that exhibit the least amount of surface area near the 6 and 12 o'clock surface orientations, such as the circle, ellipse, diamond, pentagon, and hexagon show the lowest area averaged arithmetic mean roughness compared to the other channel shapes. As seen in Figure 6, the diamond has the lowest value of arithmetic mean roughness resulting from only a small area being exposed to the 12 and 6 o'clock surface orientation.

CHANNEL PERFORMANCE MEASUREMENTS

Pressure loss and bulk convection coefficients of the channel shapes were measured over a range of Reynolds numbers using an experimental rig similar to that previously used [3,4,31] as shown in Figure 7. The experimental rig has been described in great detail and benchmarked by several investigators [3,4,31].

Darcy friction factor measurements were calculated using measured pressure drops, mass flow rates, and channel geometry dimensions taken from CT scans. During friction factor tests the entrance pressure was set to 689 kPa absolute while the exit pressure ranged from 607 kPa to 661 kPa for the different channel shapes. Inlet loss coefficients were calculated using an area ratio between the channel inlet and plenum inlet while the outlet loss coefficients were one as described by Munson et al. [32]. The mass flow rate was measured upstream of the coupons using a laminar flow element along with pressure and temperature measurements. The friction factor measurements were taken in the incompressible regime where coupon exit Mach numbers were below 0.2. To achieve high Reynolds numbers in the fully turbulent regime, the backflow pressure was regulated to control the exit Mach number ensuring incompressible flow conditions.

Convective heat transfer coefficients were calculated using data measured from the same rig shown in Figure 7. A constant channel surface temperature boundary condition was achieved by a copper block being placed between a heater and the coupon surface. During the heat transfer tests the inlet temperature was at 296K while the exit temperatures ranged from 305 K to 322 K for the different channel shapes. The power supplied by the top and bottom heaters were matched within 2.5%. A detailed description of the heat transfer measurement method is described by Stimpson et al. [5]. The same 9.77 ± 0.49 W/mK thermal conductivity of an additive Inconel 718 material measured by Wildgoose et al. [6] was used for the coupon surface temperature

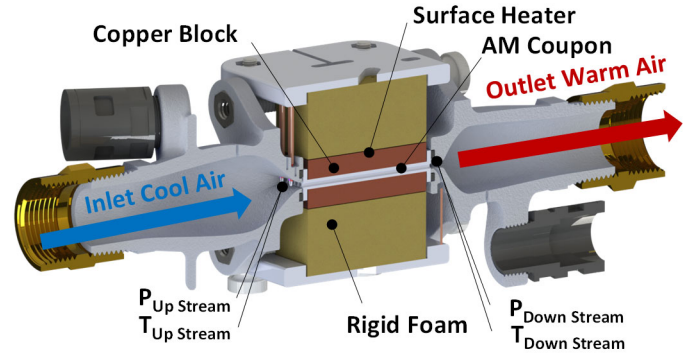


Figure 7. Experimental rig used for static pressure drop and bulk convection coefficient measurements.

calculation. A one-dimensional conduction analysis using thermocouples placed inside the copper blocks was used to calculate the surface temperature of the coupon channels.

Conduction losses through the rigid foam and plenums were measured and accounted for in the heat transfer measurements. The combined total of conduction losses through the rigid foam and plenums were less than 1% of the total power supplied by both heaters at high and low Reynolds numbers. The difference between the energy supplied by the heaters, Q_{heat} , and that transported by the air, Q_{air} , after accounting for the conduction losses was within 10.5% for the highest Reynolds numbers and within 5.7% for the lowest Reynolds numbers for all the channel shapes.

EXPERIMENTAL UNCERTAINTY

The propagation of uncertainty method was used to calculate friction factor and heat transfer experimental uncertainty as described by Figliola and Beasley [33]. Hydraulic diameter and pressure drop contributed to friction factor uncertainty the most. The uncertainty in friction factor at high Reynolds numbers was 4% while it was 9% at the lowest Reynolds numbers in the laminar regime. Reynolds number uncertainty was between 3% and 5%. Thermocouple exit temperature and hydraulic diameter were the main contributors to Nusselt number uncertainty. While the experimental uncertainty was 7% for Nusselt number, the repeatability in the measurements for the rectangle and circle was better than 2% across the range of Reynolds numbers evaluated.

COMPUTATIONAL FLUID DYNAMICS SIMULATIONS

Computational fluid dynamics (CFD) simulations were conducted on four channel shapes to complement and gain a further understanding of the experimental pressure loss and heat transfer results. The triangle, trapezoid, square, and pentagon channel shapes were selected for evaluation since these shapes show different surface roughness's and experimental pressure loss and heat transfer performances. The single channel steady Reynolds Averaged Navier Stokes (RANS) simulations were completed in ANSYS Fluent [34]. In order to capture the secondary flows of the noncircular channel shapes, the turbulence model was a Baseline Reynolds Stress Model (BSL-RSM). The design intent geometry of the four channel shapes were used for the simulation. The length of the channels matched the length of the experimental coupons. The simulations did not model or include surface roughness since the goal of the simulations are to gain further insights into the cooling performance caused by the shape of the channel without the effect of roughness.

Similar to the experimental heat transfer tests, a constant surface temperature boundary condition was imposed on the surface of the channel. The channel shapes included an inlet mass flow boundary condition and outlet outflow boundary condition. The mass flow inlet was controlled such that the simulations were conducted at a $Re_{Dh} = 20,000$ and $Re_{\sqrt{A_c}} = 20,000$ for each channel shape. The Nusselt numbers reported were calculated using the mass averaged mean temperature in the thermally fully developed regime.

The fluid domain of the channels was meshed using tetrahedral elements and inflation layers. The grids were generated with a y^+ value of one in the near wall regions. A grid independence study was performed by varying the number of cells in the fluid domain for the square channel. There was less than a 0.2% difference in Nusselt number of the square channel when going from 10M to 4M cells. The number of cells for each of the channel shapes evaluated were between 10M to 15M cells.

PRESSURE LOSS MEASUREMENTS

To cover a wide range of Reynolds numbers for each coupon, pressure loss measurements were recorded in the laminar, transitional, and fully turbulent regimes as seen in Figure 8. Noncircular hydraulically smooth channel data compiled by Duan et al. [7] is included in Figure 8 for hydraulically smooth channels. Also shown in Figure 8 is friction factor of a smooth circular channel coupon, created using a non-additive technique, that was used to benchmark the experimental rig. The friction factor of the smooth circular channel coupon agrees with the well-accepted Colebrook friction factor correlation, equation (2).

$$\frac{1}{\sqrt{f}} = -2 \log_{10} \left(\frac{K_s}{3.7D_h} + \frac{2.51}{Re\sqrt{f}} \right) \quad (2)$$

Consistent with results for AM internal passages [3–6], friction factors of the coupons are significantly higher than smooth channels due to surface roughness from the AM process as shown in Figure 8. AM coupons transition to turbulence at a much lower Reynolds number than the smooth benchmark coupon. The data in Figure 8 indicates that the square channel has a lower critical Reynolds number compared to the diamond, which may not be expected given these are the same shape. However, recall that the square channel contained a significantly higher arithmetic mean roughness compared to the diamond as shown in Figure 6. The highest friction factors in Figure 8 are observed for channel shapes with more horizontally (6 and 12 o'clock) oriented surfaces, Figure 4(f-i), due to 12 and 6 o'clock surfaces containing higher arithmetic mean roughness values compared to 3 and 9 o'clock surfaces as seen in Figure 5(a-e).

As another example to that of the square and diamond, consider the comparisons of the friction factors of the hexagon and diamond, it was expected that the hexagon would exhibit a similar or smaller friction factor compared to the diamond because the hexagon has similar variations in geometric dimensions and a larger hydraulic diameter. However, as seen in Figure 8 the hexagon contains a higher friction factor relative to the diamond because as seen in Figure 5 the arithmetic mean roughness of certain surfaces of the hexagon are two times higher than the diamond surfaces. The surface roughness results from Figure 5 and cross-sectional slices from Figure 4 also explain the reason the pentagon has a higher friction factor compared to the diamond. The pentagon contains a higher arithmetic mean

roughness and a wider spread in centroids compared to the diamond, causing the pentagon's friction factor to be higher.

Similar to the scatter in friction factor measurements of the hydraulically smooth noncircular data from Duan et al. [7], the friction factor of the additive channels varies by as much as 31% at a single Reynolds number. Efforts to scale and reduce the scatter in fRe_{Dh} between the channel shapes were made by applying a different characteristic length scale to Reynolds number. It is important to note that the calculation of friction factor still used the hydraulic diameter. Duan et al. [7] observed that using the square root of cross-sectional area as a characteristic length better scales friction factor results across a range of hydraulically smooth channel shapes compared to using hydraulic diameter. Observed in Figure 8, the triangular channels from Duan et al. [7] shows a 20% lower fRe_{Dh} relative to a circular channel that shares the same hydraulic diameter as the triangle. As seen in Figure 9, the scatter of the same two channel shapes (circle and triangle) reduces to 6% when using $fRe_{\sqrt{A_c}}$.

Figure 9 shows data for the square, trapezoid, rectangle, and triangle exhibiting a higher $fRe_{\sqrt{A_c}}$ compared to the circle, hexagon, pentagon, ellipse, and diamond. The friction factor in Figure 8 and Figure 9 is the same value while the characteristic length for Reynolds number is different. Using the square root of cross-sectional area provides similar scatter as using hydraulic diameter. The difference in fRe_{Dh} between all the channel shapes at $Re_{Dh} = 20,000$ is 31% while the difference in $fRe_{\sqrt{A_c}}$ between all the channel shapes is 32% at $Re_{\sqrt{A_c}} = 20,000$. The area scaling parameter proposed by Duan et al. [7] appears to be a better characteristic length in terms of scaling smooth noncircular channels compared to additively made channels as shown in Figure 9.

Predicted friction factor CFD results of the square, triangle, trapezoid, and pentagon are shown in Figure 8 and Figure 9. The predicted friction factor results do not follow the same trends as the experimental results. More specifically, the experimental friction factor was the highest for the square followed by the trapezoid, triangle, and pentagon. While for the predicted friction factor results shown in Figure 8 and Figure 9, the pentagon exhibits the highest friction factor followed by the square, trapezoid, and triangle. The reason for the difference in order of friction factor trends between the predicted and AM shapes is due to the differences in arithmetic mean roughness present in the AM channel shapes. In contrast to the experimental friction factor results, using the square root of cross-sectional area better scales the predicted friction factor for the square, triangle, trapezoid, pentagon compared to using hydraulic diameter. For the predicted results there is an 7% difference in friction factor between the channel shapes when using hydraulic diameter compared to a 2% difference when using square root of cross-sectional area as the characteristic length scale.

It would be anticipated that the roughness-to-hydraulic diameter ratio, R_a/D_h , is the cause for the failure to adequately scale the friction factor of the different channel shapes. However, this is not true as seen by the ellipse and circle sharing the same friction factor even though the ellipse contains a 34% lower roughness-to-hydraulic diameter ratio as seen in Table 1. Additionally, the rectangle and triangle also share the same friction factor even though the rectangle has a lower roughness-to-hydraulic diameter ratio.

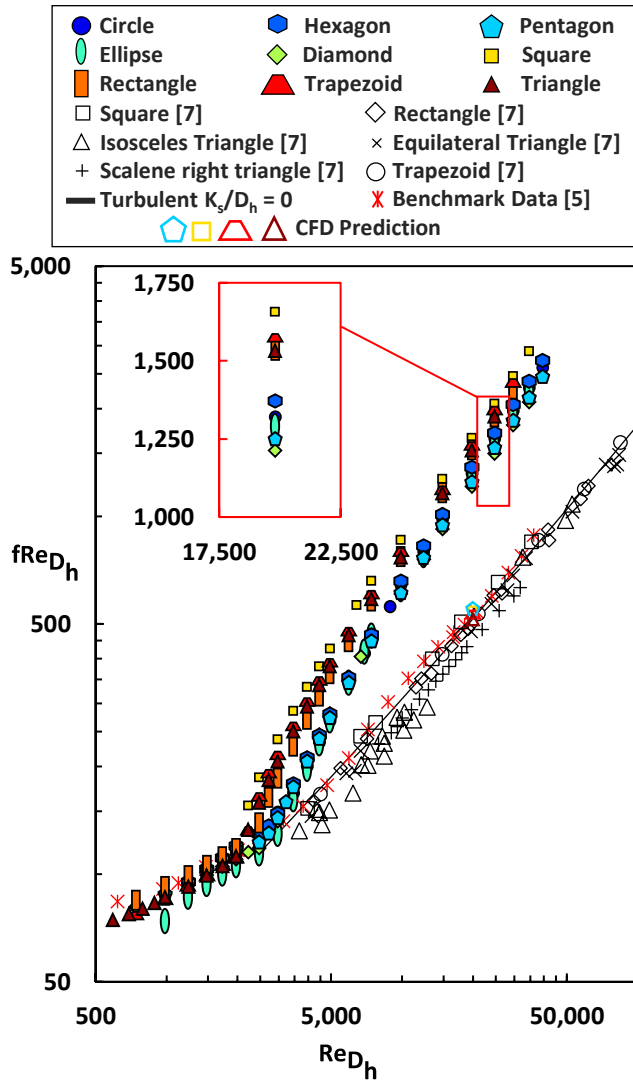


Figure 8. Friction factor data over a range of Reynolds numbers calculated using hydraulic diameter with benchmark data from Stimpson et al. [5] and smooth noncircular data compiled by Duan et al. [7].

These discrepancies reveal that the roughness-to-hydraulic diameter ratio was not the sole cause for the differences in friction factor. Accordingly, the impact of the ratio of secondary flows to the relative roughness could be one of the leading causes for the failure of hydraulic diameter and square root of cross-sectional area to scale the friction factor data.

HEAT TRANSFER EVALUATION

Similar to pressure losses, the bulk heat transfer was measured over a range of fully turbulent Reynolds numbers as shown in Figure 10. Nusselt number and Reynolds number in Figure 10 was calculated using hydraulic diameter as the length scale. The same smooth coupon used to benchmark friction factor was also used to benchmark Nusselt number. As seen in Figure 10, the smooth benchmark coupon matches Gnielinski's correlation, shown in Equation (3), for a hydraulically smooth channel.

$$Nu = \frac{f/8(Re-1000)Pr}{1+12.7\sqrt{f/8}(Pr^{2/3}-1)} \quad (3)$$

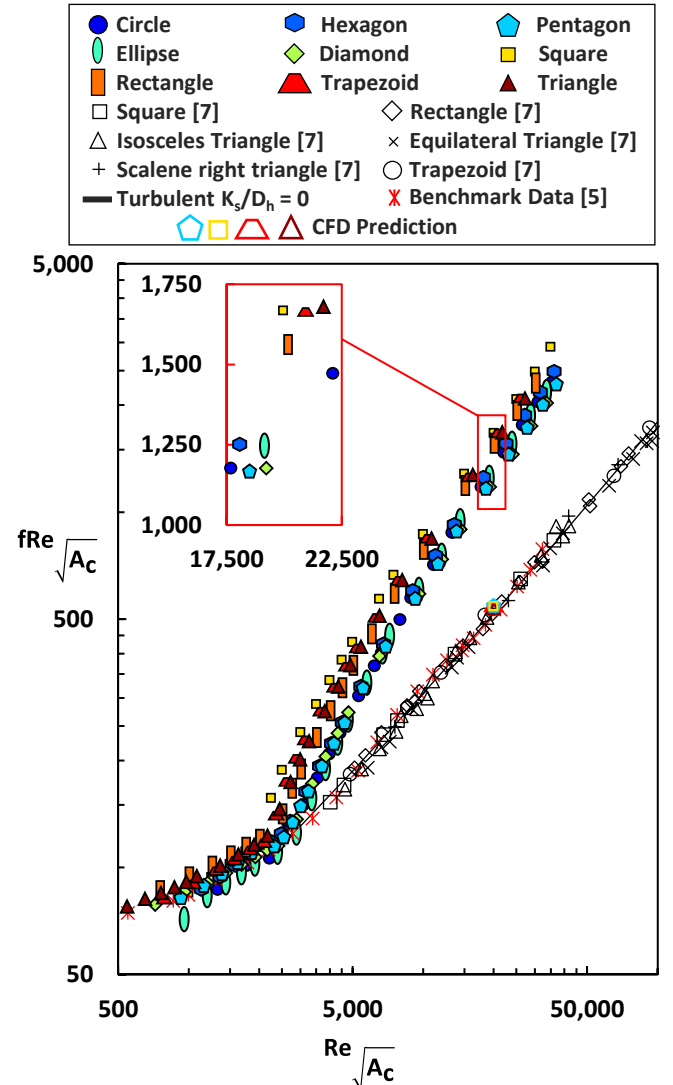


Figure 9. Friction factor data over a range of Reynolds numbers calculated using square root of cross-sectional area with benchmark data from Stimpson et al. [5] and smooth noncircular data compiled by Duan et al. [7].

Of the evaluated channel shapes, the square exhibited the highest Nusselt number and friction factor across the range of Reynolds numbers tested. It was expected that similar to the friction factors, higher surface roughness would result in higher Nusselt numbers; however, this trend was not observed with the triangle and rectangle. Although the triangle and rectangle have higher friction factors compared to the circle, diamond, ellipse, hexagon, and pentagon, the triangle and rectangle's Nusselt numbers were the same value as the mentioned shapes.

For a given Reynolds number there is a 13% difference in Nusselt number across the channel shapes for the experimental results when using hydraulic diameter as the length scale. The numerical results from Wang et al. [10] showed that using hydraulic diameter for a variety of hydraulically smooth polygonal channels lead to large errors in Nusselt number when predicted using correlations such as Gnielinski's correlation developed with circular channel datasets. Similar to the analysis of scaling friction factor results, a comparative analysis was performed between the use of the square root of cross-sectional area and hydraulic diameter for the characteristic length in Reynolds number and Nusselt number.

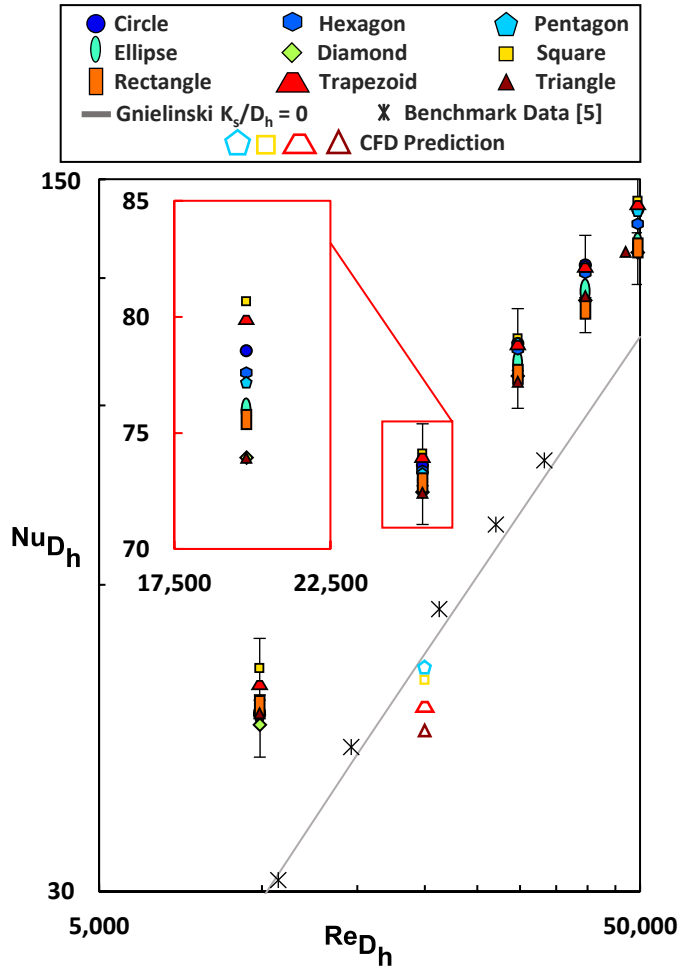


Figure 10. Nusselt number data calculated using hydraulic diameter as the characteristic length scale along with numerical data and benchmark results from Stimpson et al. [5].

Like the friction factor trends in Figure 8 and Figure 9, Figure 11 shows that using the square root of cross-sectional area results in a similar spread and scaling for Nusselt number data between all the channel shapes compared to using hydraulic diameter as the length scale in the Reynolds number. In more detail, the difference between the highest and lowest experimental Nusselt number at a shared Reynolds number, $Re_{D_h} = 20,000$, when using hydraulic diameter is 9% while when using the square root of cross-sectional area the largest difference is also 9% at $Re_{\sqrt{A_c}} = 20,000$. The Nusselt number of some channel shapes such as the circle scaled significantly better using the square root of cross-sectional area compared to hydraulic diameter. More specifically, the Nusselt number of the circle using the square root of cross-sectional area, is 2% different than the diamond relative to being 6% different than the diamond when using the hydraulic diameter as the length scale. For both Figure 10 and Figure 11, the square and trapezoid contain the highest Nusselt numbers compared to the other channel shapes.

Also shown in Figure 10 and Figure 11 are the predicted Nusselt number results from the CFD simulations of smooth square, trapezoid, triangle, and pentagon channel shapes. The predictions of the different channel shapes in Figure 10 were performed all at the same Reynolds number of $Re_{D_h} = 20,000$ while in Figure 11 the predictions were performed at a shared Reynolds number of $Re_{\sqrt{A_c}} = 20,000$.

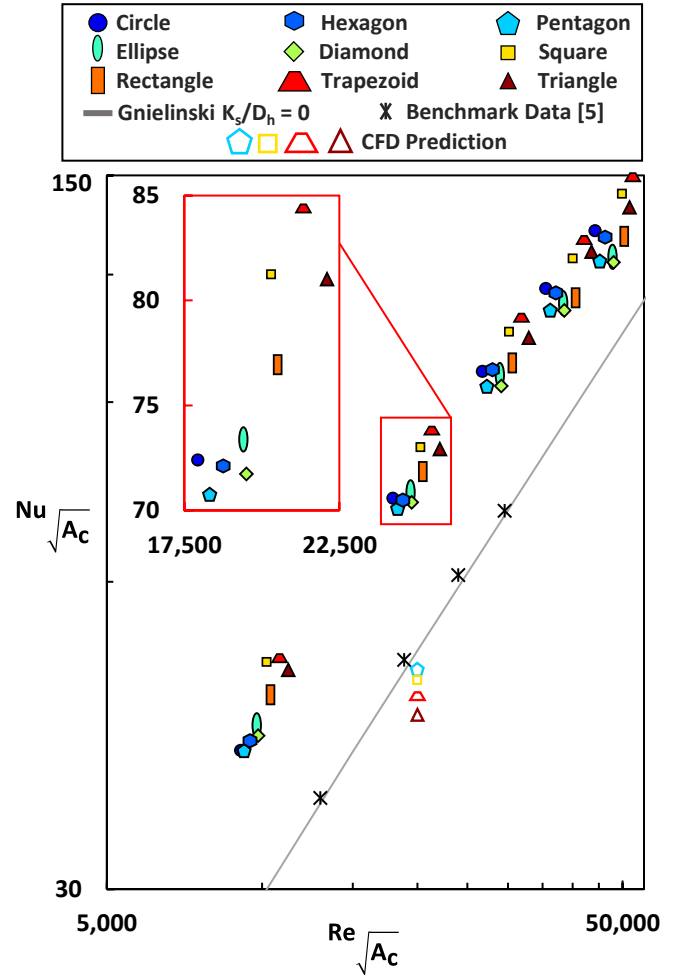


Figure 11. Nusselt number data calculated using square root of cross-sectional area as the characteristic length scale along with numerical data and benchmark results from Stimpson et al. [5].

Similar to the friction factor predictions, the square root of cross-sectional area only slightly better scales the predicted Nusselt number compared to hydraulic diameter. More specifically, the scatter for predicted Nusselt number data when using hydraulic diameter is 14% at $Re_{D_h} = 20,000$ while when using the square root of cross-sectional area the scatter is reduced to 10% at $Re_{\sqrt{A_c}} = 20,000$ between the evaluated channel shapes.

Matching the predicted friction factor results, the predicted results in Figure 10 and Figure 11 show that the pentagon exhibits the highest Nusselt number followed by the square, trapezoid, and triangle. However, the predictions do not fully match experimental trends in Nusselt number. The predicted data shows that the pentagon contains the highest Nusselt number of the four channel shapes while the experimental results show that the pentagon has the third highest Nusselt number out of the four channel shapes. The reason for the discrepancy is a result of the differences in arithmetic mean roughness between the channel shapes that the CFD predictions do not model. The square, trapezoid, and triangle shapes contain roughness levels 40% to 60% higher than the pentagon as seen in Figure 6. The higher surface roughness leads to increases in turbulent mixing causing an increase in the Nusselt number for the square, trapezoid, and triangle channel shape's relative to the pentagon. Furthermore, the square, trapezoid, and triangle shapes also contain higher

roughness-to-hydraulic diameter ratios as seen in Table 1 compared to the pentagon.

Nondimensionalized temperature contours and secondary flow vectors of the numerical data can be seen in Figure 12. The temperature is normalized using the surface temperature and mean flow temperature while the secondary flow velocities are nondimensionalized by the mean streamwise velocity. Similar to literature [35,36], Figure 12 shows that as the number of sides in a channel increases, there is a higher number of secondary circulation zones and the strength of the circulation zones decrease.

The convective heat transfer near the corners of the channel shapes are lower compared to the area between the corners as a result of a lower velocity at the channel corners. This result agrees with Wang et al. [10], who describes the corners as inducing a blocking effect which lowers the local heat transfer. As the corner angle decreases, such as going from a pentagon to triangle as seen in Figure 12, the local heat transfer near the corner reduces. The local heat transfer between the corners increases as the number of sides decrease as seen by the temperature contours in Figure 12.

The augmentations of Nusselt number and friction factor relative to smooth correlations, Equation (3), are seen in Figure 13. The ellipse, diamond, circle, hexagon, and pentagon exhibited lower friction factor augmentation for an identical Nusselt augmentation compared to the rectangle and triangle. Nusselt number and friction factor augmentations for all the channel shapes are between the square and diamond shapes, signifying that roughness and surface deformations are significant contributors to friction factor and Nusselt number augmentation.

The ellipse, hexagon, circle, diamond, and pentagon contain the same Nusselt number augmentation as the rectangle and triangle for a lower pressure drop penalty at a given Reynolds number. The pentagon contains the same Nusselt number augmentation as the triangle even though the pentagon has a 21% lower friction factor at the same Reynolds numbers.

As seen in Figure 14, Nusselt number and friction factor of the channel shapes are compared to that of the circular channel. The pentagon is the highest performing channel shape relative to the circle, since the pentagon contains a 4% lower friction factor for an equal Nusselt number as the circular channel. The square friction factor augmentation is 25% higher compared to the circle while the square's Nusselt augmentation is only 3% higher at most Reynolds numbers compared to the circle.

CONCLUSION

Nine channel shapes (circle, hexagon, pentagon, ellipse, diamond, square, rectangle, trapezoid, and triangle) which shared the same cross-sectional perimeter were manufactured in the 90° (vertical) build orientation using DMLS. The channels were CT scanned to evaluate their geometric dimensions and surface roughness. Pressure loss and heat transfer measurements of the different channel shapes were evaluated over a range of Reynolds numbers. In addition to the experimental measurements, pressure loss and heat transfer CFD predictions were conducted on the square, trapezoid, pentagon, and triangle channel shapes.

The results presented in this paper show that regardless of channel shape, the as-built channel geometries printed larger than their hydraulic diameter, perimeter, and cross-sectional area design intent. The perimeter of an AM channel is closer to its design intent compared to cross-sectional area regardless of channel shape. There are more variations in a channel's perimeter compared to cross-sectional area.

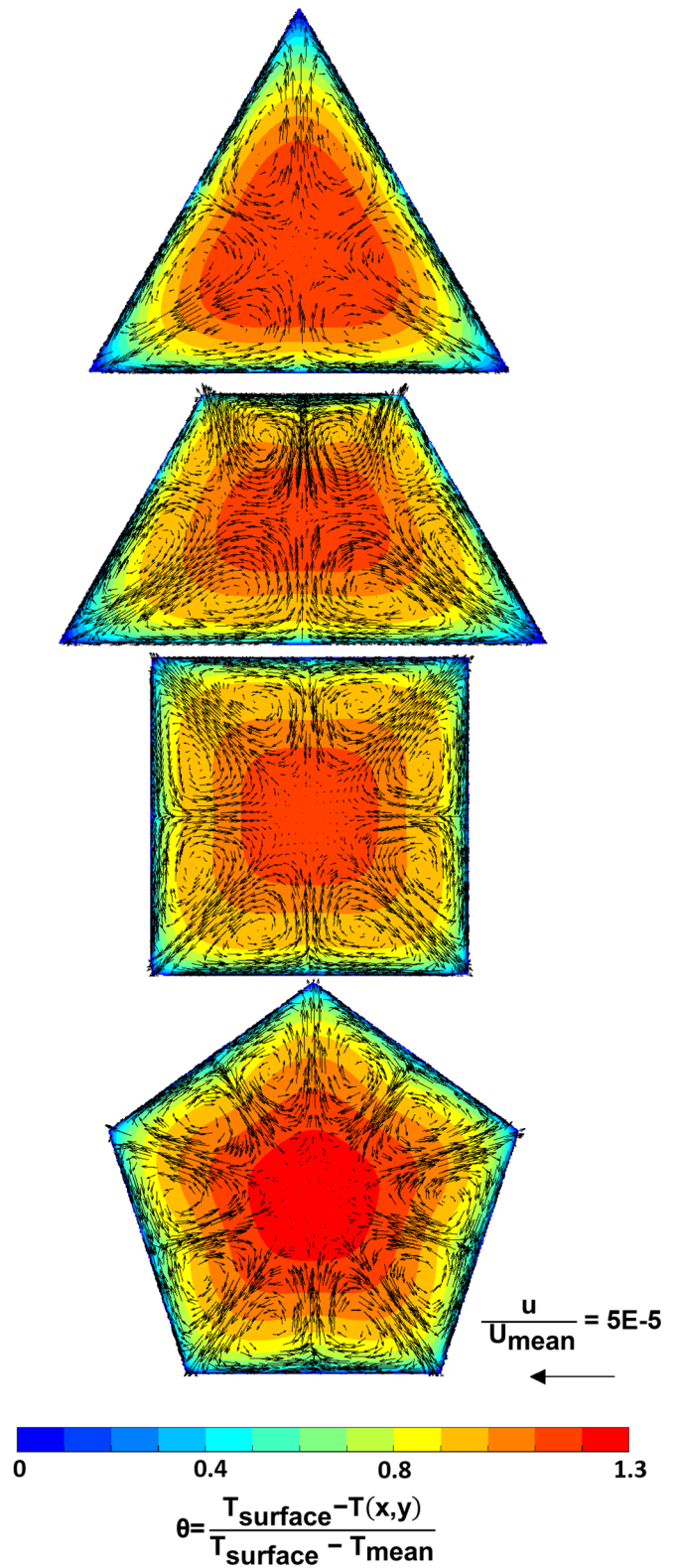


Figure 12. Nondimensionalized temperature contours with secondary flow vectors of the triangle, trapezoid, square, and pentagon channel shapes.

The square, triangle, trapezoid, and rectangle exhibited the largest deviations in geometry and surface roughness resulting in the highest friction factors. Characteristic length scales such as hydraulic diameter and square root of cross-sectional area were evaluated for both friction factor and Nusselt number. Unlike

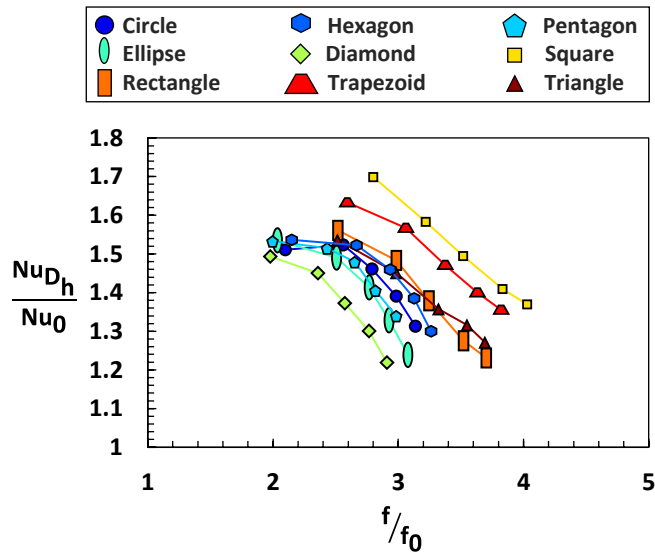


Figure 13. Nusselt number and friction factor augmented by a hydraulically smooth channel for the different channel shapes over a range of fully turbulent Reynolds numbers.

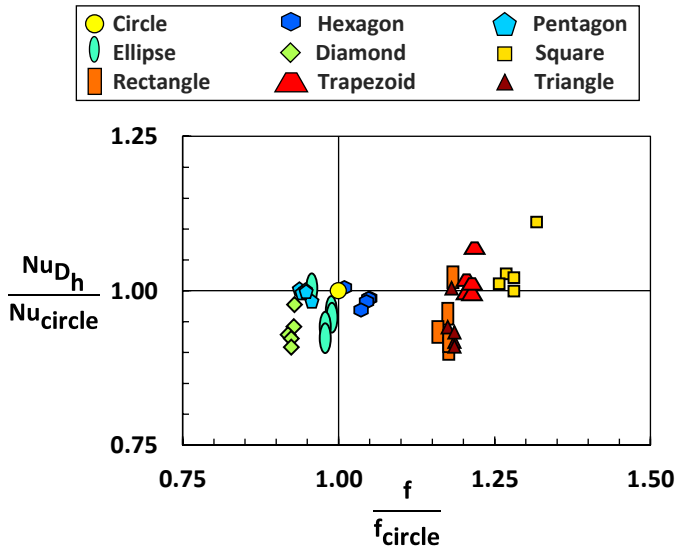


Figure 14. Nusselt number and friction factor of channel shapes augmented by the Nusselt number and friction factor of the circular channel shape at the same Reynolds number.

noncircular hydraulically smooth channels, there was no reduction in the scatter or differences in scaling of friction factor or heat transfer results when using hydraulic diameter or square root of cross-sectional area between the additively made channel shapes. The experimental results reveal that the pentagon showed the best performance between pressure loss and heat transfer compared to the circular channel. The trapezoid and square contained the largest Nusselt number and friction factor augmentations of the evaluated shapes.

Additive manufacturing can be used as a tool to fabricate complex internal passages, however designers using the process need to consider the surface deformation and roughness attributed to the geometry of a passage. There is a fundamental need to address the best scaling parameter of cooling performance for non-conventional shapes, so that the next generation of AM enabled cooling channel designs can be developed and fairly

evaluated. Understanding the impact a channel shape has on its pressure losses and convective heat transfer will allow designers to fully utilize the design freedom and added performance when using the additive process.

ACKNOWLEDGMENT

The authors would like to acknowledge the funding provided by the U.S. Department of Energy National Energy Technology Laboratory. As well as recognize the collaborative efforts in manufacturing the coupons with Corey Dickman and members at Penn State's CIMP-3D lab. The authors thank Timothy Stecko and Whitney Yetter for carrying out the CT scans. This paper is based upon work supported by the Department of Energy under Award Number DE-FE0031760.

This report was prepared as an account of work sponsored by an agency of the United States Government. Neither the United States Government nor any agency thereof, nor any of their employees, makes any warranty, express or implied, or assumes any legal liability or responsibility for the accuracy, completeness, or usefulness of any information, apparatus, product, or process disclosed, or represents that its use would not infringe privately owned rights. Reference herein to any specific commercial product, process, or service by trade name, trademark, manufacturer, or otherwise does not necessarily constitute or imply its endorsement, recommendation, or favoring by the United States Government or any agency thereof. The views and opinions of authors expressed herein do not necessarily state or reflect those of the United States Government or any agency thereof.

REFERENCES

- [1] Liang, D., He, G., Chen, W., Chen, Y., and Chyu, M. K., 2022, "Fluid Flow and Heat Transfer Performance for Micro-Lattice Structures Fabricated by Selective Laser Melting," *Int. J. Therm. Sci.*, **172**, p. 107312.
- [2] Parbat, S., Min, Z., Yang, L., and Chyu, M., 2020, "Experimental and Numerical Analysis of Additively Manufactured Inconel 718 Coupons with Lattice Structure," *J. Turbomach.*, **142**(6).
- [3] Kirsch, K. L., and Thole, K. A., 2018, "Experimental Investigation of Numerically Optimized Wavy Microchannels Created through Additive Manufacturing," *J. Turbomach.*, **140**(2).
- [4] Snyder, J. C., Stimpson, C. K., Thole, K. A., and Mongillo, D., 2016, "Build Direction Effects on Additively Manufactured Channels," *J. Turbomach.*, **138**(5), p. 051006.
- [5] Stimpson, C. K., Snyder, J. C., Thole, K. A., and Mongillo, D., 2016, "Scaling Roughness Effects on Pressure Loss and Heat Transfer of Additively Manufactured Channels," *J. Turbomach.*, **139**(2), p. 021003.
- [6] Wildgoose, A. J., Thole, K. A., Sanders, P., and Wang, L., 2021, "Impact of Additive Manufacturing on Internal Cooling Channels with Varying Diameters and Build Directions," *J. Turbomach.*, **143**(7).
- [7] Duan, Z., Yovanovich, M. M., and Muzychka, Y. S., 2012, "Pressure Drop for Fully Developed Turbulent Flow in Circular and Noncircular Ducts," *J. Fluids Eng. Trans. ASME*, **134**(6).
- [8] Sarmiento, A. P. C., Soares, V. H. T., Milanez, F. H., and Mantelli, M. B. H., 2020, "Heat Transfer Correlation for Circular and Non-Circular Ducts in the Transition Regime," *Int. J. Heat Mass Transf.*, **149**, p. 119165.
- [9] McHale, J. P., and Garimella, S. V., 2010, "Heat Transfer in Trapezoidal Microchannels of Various Aspect Ratios," *Int. J. Heat Mass Transf.*, **53**(1–3), pp. 365–375.
- [10] Wang, P., Yang, M., Wang, Z., and Zhang, Y., 2014, "A New Heat Transfer Correlation for Turbulent Flow of Air with

- Variable Properties in Noncircular Ducts,” J. Heat Transfer, **136**(10).
- [11] Muzychka, Y. S., and Yovanovich, M. M., 2009, “Pressure Drop in Laminar Developing Flow in Noncircular Ducts: A Scaling and Modeling Approach,” J. Fluids Eng. Trans. ASME, **131**(11), pp. 1111051–11110511.
- [12] Nikuradse, J., 1926, “Untersuchungen Über Die Geschwindigkeitsverteilung in Turbulenten Stromungen,” VDI-Forschungsheft, No. **281**.
- [13] Leung, C. W., and Probert, S. D., 1997, “Forced-Convective Turbulent-Flows through Horizontal Ducts with Isosceles-Triangular Internal Cross-Sections,” Appl. Energy, **57**(1), pp. 13–24.
- [14] Kays, W. M., Crawford, M. E., and Bernhard, W., 2005, *Convective Heat and Mass Transfer*, McGraw-Hill, Boston.
- [15] Jones, O. C., 1976, “An Improvement in the Calculation of Turbulent Friction in Rectangular Ducts,” J. Fluids Eng.
- [16] Duan, Z., 2012, “New Correlative Models for Fully Developed Turbulent Heat and Mass Transfer in Circular and Noncircular Ducts,” J. Heat Transfer, **134**(1).
- [17] Leung, C. W., Wong, T. T., and Kang, H. J., 1998, “Forced Convection of Turbulent Flow in Triangular Ducts with Different Angles and Surface Roughnesses,” Heat Mass Transf. und Stoffuebertragung, **34**(1), pp. 63–68.
- [18] Snyder, J. C., Stimpson, C. K., Thole, K. A., and Mongillo, D. J., 2015, “Build Direction Effects on Microchannel Tolerance and Surface Roughness,” J. Mech. Des. Trans. ASME, **137**(11), p. 111411.
- [19] Klingaa, C. G., Bjerre, M. K., Baier, S., De Chiffre, L., Mohanty, S., and Hattel, J. H., 2019, “Roughness Investigation of SLM Manufactured Conformal Cooling Channels Using X-Ray Computed Tomography,” *9th Conference on Industrial Computer Tomography*.
- [20] Zhang, B., Li, L., and Anand, S., 2020, “Distortion Prediction and NURBS Based Geometry Compensation for Reducing Part Errors in Additive Manufacturing,” Procedia Manuf., **48**, pp. 706–717.
- [21] Kamat, A. M., and Pei, Y., 2019, “An Analytical Method to Predict and Compensate for Residual Stress-Induced Deformation in Overhanging Regions of Internal Channels Fabricated Using Powder Bed Fusion,” Addit. Manuf.
- [22] Thole, K. A., Lynch, S., and Wildgoose, A. J., 2021, “Review of Advances in Convective Heat Transfer Developed through Additive Manufacturing,” Adv. Heat Transf., **53**.
- [23] EOS, 2011, *Technical Description EOSINT M 280*.
- [24] Kleszczynski, S., Ladewig, A., Friedberger, K., Jacobsmuhlen, J. zur, Merhof, D., and G. W., 2015, “Position Dependency of Surface Roughness in Parts From Laser Beam,” *SFF Symp. Proc.*, pp. 360–370.
- [25] Volume Graphics, 2021, “VGStudio MAX.”
- [26] Reinhart, C., 2011, *Industrial CT & Precision*, Volume Graphics GmbH, Heidelberg, Germany.
- [27] Wildgoose, A. J., Thole, K. A., Subramanian, R., Kerating, L., and Kulkarni, A., 2022, “Impacts of the Additive Manufacturing Process on the Roughness of Engine Scale Vanes and Cooling Channels,” Under Rev. Proc. ASME Turbo Expo, GT2022-82298.
- [28] Klingaa, C. G., Bjerre, M. K., Baier, S., De Chiffre, L., Mohanty, S., and Hattel, J. H., 2019, “Roughness Investigation of SLM Manufactured Conformal Cooling Channels Using X-Ray Computed Tomography,” *9th Conference on Industrial Computer Tomography*.
- [29] Snyder, J. C., Stimpson, C. K., Thole, K. A., and Mongillo, D. J., 2015, “Build Direction Effects on Microchannel Tolerance and Surface Roughness,” J. Mech. Des. Trans. ASME, **137**(11), p. 111411.
- [30] Klingaa, C. G., Dahmen, T., Baier-Stegmaier, S., Mohanty, S., and Hattel, J. H., 2020, “Investigation of the Roughness Variation along the Length of LPBF Manufactured Straight Channels,” Nondestruct. Test. Eval., **35**(3), pp. 304–314.
- [31] Stimpson, C. K., Snyder, J. C., Thole, K. A., and Mongillo, D., 2016, “Roughness Effects on Flow and Heat Transfer for Additively Manufactured Channels,” J. Turbomach., **138**(5), p. 051008.
- [32] Munson, R. B., Young, D. F., and Okiishi, T. H., 1990, *Fundamentals of Fluid Mechanics*, Wiley & Sons, Hoboken, NJ.
- [33] Figliola, R. S., and Beasley, D. E., 2005, *Theory and Design for Mechanical Measurements*, Wiley & Sons, Hoboken, Nj.
- [34] ANSYS, 2020, *ANSYS FLUENT*, Canonsburg, PA.
- [35] Deprati, F., 2021, “Direct Numerical Simulation of Flow and Heat Transfer in Complex Ducts,” Aerotec. Missili Spaz., **100**, pp. 263–276.
- [36] Li, Y. K., Zheng, Z. Y., Zhang, H. N., Li, F. C., Qian, S., Joo, S. W., and Kulagina, L. V., 2017, “Numerical Study on Secondary Flows of Viscoelastic Fluids in Straight Ducts: Origin Analysis and Parametric Effects,” Comput. Fluids, **152**, pp. 57–73.